A comparative study for H$_2$–CH$_4$ mixture wettability in sandstone porous rocks relevant to underground hydrogen storage

Hashemi, Leila; Boon, Maartje; Glerum, Wuis; Farajzadeh, Rouhi; Hajibeygi, Hadi

Citation (APA)
Hashemi, L., Boon, M., Glerum, W., Farajzadeh, R., & Hajibeygi, H. (2022). A comparative study for H$_2$–CH$_4$ mixture wettability in sandstone porous rocks relevant to underground hydrogen storage. *Advances in Water Resources*, *163*, Article 104165. https://doi.org/10.1016/j.advwatres.2022.104165
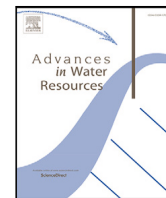
Important note
To cite this publication, please use the final published version (if applicable).
Please check the document version above.

A comparative study for H₂–CH₄ mixture wettability in sandstone porous rocks relevant to underground hydrogen storage

Leila Hashemi *, Maartje Boon, Wuis Glerum, Rouhi Farajzadeh, Hadi Hajibeygi

Faculty of Civil Engineering and Geosciences, Delft University of Technology, P.O. Box 5048, Delft, 2600 GA, The Netherlands

ABSTRACT

Characterizing the wettability of hydrogen (H_2)–methane (CH_4) mixtures in subsurface reservoirs is the first step towards understanding containment and transport properties for underground hydrogen storage (UHS). In this study, we investigate the static contact angles of H_2–CH_4 mixtures, in contact with brine and Bentheimer sandstone rock using a captive-bubble cell device at different pressures, temperatures and brine salinity values. It is found that, under the studied conditions, H_2 and CH_4 show comparable wettability behaviour with contact angles ranging between [25°–45°]; and consequently their mixtures behave similar to the pure gas systems, independent of composition, pressure, temperature and salinity. For the system at rest, the acting buoyancy and surface forces allow for theoretical sensitivity analysis for the captive-bubble cell approach to characterize the wettability. Moreover, it is theoretically validated that under similar Bond numbers and similar bubble sizes, the contact angles of H_2 and CH_4 bubbles and their mixtures are indeed comparable. Consequently, in large-scale subsurface storage systems where buoyancy and capillary are the main acting forces, H_2, CH_4 and their mixtures will have similar wettability characteristics.

1. Introduction

Development of large-scale (TWh) energy storage technologies is essential in the successful transition towards renewable energy systems. Therefore, energy has to be converted into forms that can be stored at such large scales. One of the attractive energy carriers is hydrogen (H_2), due to its high energy content per mass, 141.86 MJ/kg, and its carbon-free combustion products (Hassanpouryouzband et al., 2021). However, there exists a major challenge in development of storage technologies for hydrogen. Being the lightest molecule, its volumetric energy content is relatively low (Stone et al., 2009; Zivar et al., 2021). More specifically, it stores only about 132 KWh in 1 m³ at relatively high pressure of 50 bars and temperature of 298 K (Kabuth et al., 2017). As such, to achieve feasible large-scale storage for compressed hydrogen gas, gigantic volumes are needed. These volumes are beyond the technical, economical, land-usage, and safety scope of surface-based storage tanks (Taylor et al., 1986; Schaber et al., 2004). Underground reservoirs, on the other hand, provide giant volumes to store hydrogen in the expected TWh scales. These formations can be in the form of solution-mined salt caverns (Ramesh Kumar et al., 2021) or geological porous reservoirs (Walters, 1976; Tarkowski, 2019; Gabrielli et al., 2020), including depleted hydrocarbon fields and saline aquifers (Hashemi et al., 2021a).

There exist a few experiences with storing hydrogen or its mixture with methane in porous reservoirs (Panfilov et al., 2006; Kruck et al., 2013) and several pilot projects are currently underway (RAG, 2021; Pérez et al., 2016). However, to date, a rigorous understanding of many aspects related to subsurface storage of pure hydrogen and its mixture with methane is still lacking (Heinemann et al., 2021).

In some aspects, underground hydrogen storage (UHS) is similar to that of underground gas storage (UGS), as both are compressed gases being stored cyclically in subsurface formations. However, in many aspects, UHS is expected to behave quite differently than UGS. Firstly, H_2 is very different than CH_4 gas, in its molecular weight, diffusivity, dissolution, density and surface/interfacial tension. Secondly, the cyclic loading and frequency of the green hydrogen injection and production, supplied by the intermittent green energy production, is expected to be much different than that of UGS. Lastly, hydrogen purity is expected to be maintained during the storage period, as sensitivities towards hydrogen impurities in fuel cells are very high (Laban, 2020). These differences have recently motivated the scientific community to study hydrogen properties in detail, specially its wettability characteristics in contact with reservoir brine and rock (Iglauer et al., 2021; Hashemi et al., 2021b; Ali et al., 2021). This is due to the fact that hydrogen will come in contact with brine whether in aquifers or porous rocks

containing connate water (Hashemi et al., 2021a; Heinemann et al., 2021).

H$_2$/brine/rock wettability is a key factor in identification of the hydrogen interaction with reservoir brine and rock. More precisely, it allows for understanding the distribution of hydrogen through the porous rock micro channels. According to Young's equation, it is characterized by the contact angle between the interface of gas/brine in contact with the rock surface (De Gennes, 1985), i.e.,

$$\cos\ \theta = \frac{(\sigma_{rb} - \sigma_{rg})}{\sigma_{bg}}. \tag{1}$$

Here, $\sigma_{rb}, \sigma_{rg}, \sigma_{bg}$ correspond to the interfacial forces between each pair of the phases, respectively: rock/brine, rock/gas and brine/gas (Young, 1805).

Typically, in geological reservoirs, the adhesive forces between brine and rock are much bigger than between gas and rock, because molecules in the liquid phase are much closer to each other than in the gas phase. Therefore, the contact angle in gas/brine/rock systems is likely to be less than 90 degrees. Consequently, water-wet conditions can be expected during underground hydrogen storage. The distribution of hydrogen and brine in the porous rock influences multiphase flow properties such as relative permeability and capillary pressure. In water-wet systems, the non-wetting phase, in our case hydrogen, will preferentially flow through the larger pores resulting in a higher relative permeability. This facilitates the injectivity of the reservoir, while the amount of capillary-trapped hydrogen will be smaller. Both aspects are favourable for UHS (Alhammadi et al., 2017; Arif et al., 2019).

Wettability of the H$_2$/brine/rock system has been the focus of some recent studies, all of which were conducted using water-wet rocks (Yekta et al., 2018; van Rooijen et al., 2021; Iglauer et al., 2021; Hashemi et al., 2021b) with pure hydrogen gas. These studies collectively revealed static (Hashemi et al., 2021b) and dynamic (Yekta et al., 2018; van Rooijen et al., 2021; Iglauer et al., 2021; Ali et al., 2021) contact angles of hydrogen by different experimental methods: captive-bubble cell (Hashemi et al., 2021b; Higgs et al., 2021), tilted-plate (Iglauer et al., 2021; Ali et al., 2021), microfluidics (van Rooijen et al., 2021) and indirectly (Yekta et al., 2018) and directly (Higgs et al., 2021) through core-flooding techniques. A summary of the measured contact angles as well as the conditions and experimental techniques can be found in Table 1.

The characterization of H$_2$–CH$_4$ wettability is important for comparison of UHS and UGS. Despite its importance, there exists no rigorous study which investigates and reports how hydrogen wettability compares with that of methane and hydrogen-methane mixtures of different concentrations. In addition, there can be cases in which H$_2$ mixes with the reservoir CH$_4$, for example, if it is used as cushion gas or traces of it exists in the subsurface environment, such as depleted gas fields. Moreover, it is important for industrial applications where first H$_2$–CH$_4$ mixture is introduced in the gas grid and storage facilities. As the production of H$_2$ scales up in the future, the fraction of H$_2$ concentration in the mixture is expected to be further increased. For example, the first UHS project in Europe, Underground Sun Storage by RAG Austria AG, stored 20% H$_2$ and 80% CH$_4$ (RAG, 2017) in a porous reservoir.

Mixing of H$_2$ with CH$_4$ impacts the physio-chemical properties of the injected hydrogen and consequently its displacement process (Hassanpouryouzband et al., 2020; Tek, 2012; Simon et al., 2015; Sáinz-García et al., 2016). This can potentially impact the upscaled multiphase flow functions of capillary pressure and relative permeability (Hashemi et al., 2021a; Rücker et al., 2019; Kunz et al., 2018; Pan et al., 2021; Carden and Paterson, 1979). A correct description of these upscaled flow functions is needed to ensure the safety of underground hydrogen storage, as well as to optimize the cyclic injection and production of hydrogen. As such, characterization of the H$_2$–CH$_4$ mixture

wettability is crucially important, which is the focus of the present study.

In this work, we directly measure the static contact angles of H$_2$–CH$_4$ mixtures in contact with brine and sandstone rock using a captive-bubble cell experimental methodology (Kaveh et al., 2014; Hashemi et al., 2021b). We systematically analyse contact angles of different size gas bubbles and different mixture concentrations. By providing a modelling analysis, we validate our methodology and the findings of this study. The structure of the paper is as follows. In the Materials and Methods section, a description of the methodology and test conditions are presented in detail. This is followed by the results and interpretation of the data. A sensitivity analysis is also performed, on the basis of the Young–Laplace equation, to better analyse and justify the experimental observations. Finally, the main learning points are presented in the conclusion.

2. Materials and methods

In this study, static contact angles for H$_2$–CH$_4$ gas mixtures, as well as pure CH$_4$ gas, in contact with brine and Bentheimer sandstone rock are measured using the captive-bubble cell device (Kaveh et al., 2014; Hashemi et al., 2021b).

2.1. Materials

The gas mixtures consisted of 99.99 mol % purity H$_2$ and 99.5 mol % purity CH$_4$ both produced by Linde-gas Company. The gas mixture was prepared by filling up the pump with both gases in the desired concentration at the desired pressure, having the pump with the gasses stand for one day so to allow for a fully-mixed gas-liquid system. The brines were made by dissolving NaCl in deionized water. A Bentheimer sandstone rock slab with dimensions of 30 × 6 × 12 mm was used in the experiments. The sample was untreated and cut from the same clean Bentheimer sandstone block as in the Bentheimer rock sample used in Hashemi et al. (2021b). The permeability of the sample was 2–3 Darcy and the porosity was around 20%. The mineral composition consisted for 95% of quartz which was evenly distributed throughout the rock matrix (Peksa et al., 2015). The surface roughness was 0.03 mm and was determined by microscopic analysis (Hashemi et al., 2021b). The experimental conditions used for each H$_2$–CH$_4$ gas mixtures and pure CH$_4$ gas can be found in Table 2.

2.2. Experimental apparatus and procedure

A schematic of the experimental apparatus can be seen in Fig. A.1 of Appendix A. It is similar to the setup used by Hashemi et al. (2021b), adapted in this study for gas mixtures. The apparatus consisted of a high pressure/high temperature single steel cell with a volume of 150 ml filled with brine. The rock sample was attached to the centre of the cell. The cell was placed in an oven to control the temperature. Brine was continuously injected at a flow rate of 0.02ml/min from the bottom of the cell. The pressure was regulated with a back-pressure device connected to the top of the cell and attached to a N$_2$ cylinder. Gas bubbles of approximately 2 mm in diameter were released from a nozzle at the bottom of the cell into the brine. The bubble buoyantly rose until it reached the rock surface. The bubble slowly dissolved and diffused into the brine resulting in bubbles of different sizes. Images with a resolution of 6.9 MP (3216 × 2136) were taken at evenly spaced time intervals using a Canon 90 camera (with a maximum resolution of 12.3 MP) attached to an endoscope. The pressure and temperature in the cell were continuously monitored. The lines of the system were thoroughly cleaned with water and ethanol at the start of each experiment to avoid any impact of contamination on the contact angle measurements.

Table 1

Overview of the reported measurements for the range of advancing (ACA), receding (RCA) and static (SCA) contact angles for H_2-brine systems. Here (S) stands for sandstone porous rock.

Measuring technique	ACA (°)	RCA (°)	SCA (°)	P (bar)	T (°C)	Brine phase	Medium
Captive-bubble cell[a]			25–45	20–100	20–50	0–50k NaCl	Bentheimer (S)/Berea (S)
Captive-bubble cell[b]			27–39	68.9–206.8	25	0–5k NaCl	Bentheimer (S)
Tilted plate[c]	0–48.3	0–44.1		50–250	23–70	100k NaCl	Quartz
Microfluidics[d]	13–39	6–23		10	20	pure water	Borosilicate glass
Indirect Core-flood[e]		21.6, 34.9		50, 100	20, 45	pure water	Vosges (S)
Direct Core-flood[b]			39.77, 59.75	6.9–172.4	25	0-2k KI	Bentheimer (S)

[a]Hashemi et al. (2021b).
[b]Higgs et al. (2021).
[c]Iglauer et al. (2021).
[d]van Rooijen et al. (2021).
[e]Yekta et al. (2018).

Table 2

Experimental conditions.

Rock phase	Gas phase	Brine phase (ppm)	Temperature (°)	Pressure (bar)
Bentheimer Sandstone	CH4	Pure water	30, 50	20, 50, 70, 100
		5k NaCl		
		50k NaCl		
	20% CH4–80% H2	Pure water	30, 50	20, 50, 70, 100
		5k NaCl		
	50% CH4–50% H2	Pure water	30, 50	20, 50, 70, 100
		5k NaCl		
	80% CH4–20% H2	Pure water	30, 50	20, 50, 70, 100
		5k NaCl		
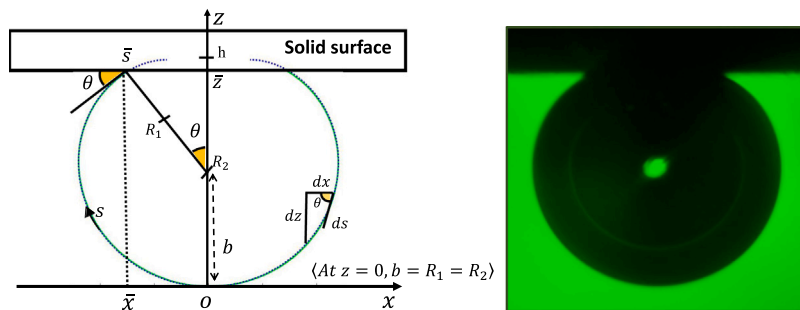
Fig. 1. Schematic of an axisymmetric gas bubble below a solid rock surface (left). The blue contour indicates the gas/brine interface. Shown on the right is an image of a H_2–CH_4 mixture bubble in contact with porous sandstone rock, captured by the camera.

2.3. Image analysis

Contact angles were derived for each of the images taken during the experiment using an in-house MATLAB code which is based on the ADSA-P technique (Li et al., 1992). The ADSA-P technique fits the best theoretical Laplacian curve on the physical observed bubble interface and is based on the Young–Laplace equation (Next section). For this purpose the images are cropped and binarized such that the interface including the apex and contact points can be detected. To find the size of the bubble, the outer diameter of the nozzle is used. The brine and gas density values used in the analysis are reported in Appendix B, Tables B.12–B.22. For more details about the image analysis procedure the reader is referred to Hashemi et al. (2021b).

2.4. Theoretical analyses based on Young–Laplace equation

Fig. 1 shows a schematic of an axisymmetric gas bubble. The blue contour indicates the gas/brine interface. The pressure difference across this interface, i.e., ΔP, can be described by the Young–Laplace equation (Li et al., 1992) as

$$\Delta P = \sigma(\frac{1}{R_1} + \frac{1}{R_2}), \tag{2}$$

where σ [N/m] is the interfacial tension and R_1 [m] and R_2 [m] are the principle radii of the curvature. The pressure difference across the

interface is due to the interfacial tension, as well as the force of gravity, i.e.,

$$\Delta P = \Delta P_0 + \Delta P_g. \tag{3}$$

At gravity-capillary equilibrium, the pressure difference across the interface can be described as a function of depth, z [m], i.e.,

$$\Delta P = \Delta P_0 + \Delta\rho g z. \tag{4}$$

Here, $\Delta\rho$ [kg/m³] is the density difference between the gas and the brine phase, and g [m/s²] is the gravitational acceleration. Since the apex point is taken as the reference, i.e., $z = 0$, no gravity term is considered there and thus one can write $R_1 = R_2 = b$ at this point. Therefore, at the apex point, Eq. (2) can be written as

$$\Delta P_{apex} = \frac{2\sigma}{b}. \tag{5}$$

By substituting Eq. (4) into Eq. (2) it is found that

$$\sigma(\frac{1}{R_1} + \frac{1}{R_2}) = \frac{2\sigma}{b} + \Delta\rho g z \tag{6}$$

holds for any depth (z). In cylindrical coordinate, one can write

$$\frac{1}{R_1} = \frac{d\theta}{ds} \tag{7}$$

and

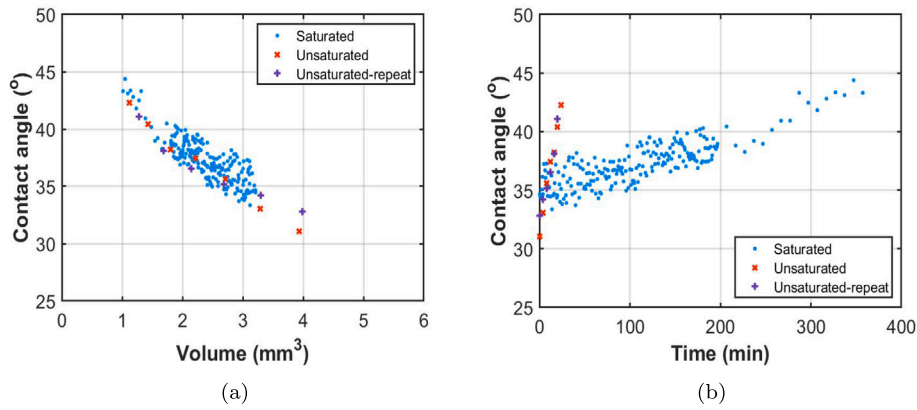$$\frac{1}{R_2} = \frac{\sin\theta}{x}. \tag{8}$$

Fig. 2. Contact angle versus volume (a) and time (b) for a system where the brine was highly saturated with hydrogen (blue dots) and a system where the brine was unsaturated (red and purple dots). For the experiment with the highly saturated brine images were taken every minute for the first 197 min, after which images were taken every 10 min. For the experiments with unsaturated brine images were taken every 4 min.
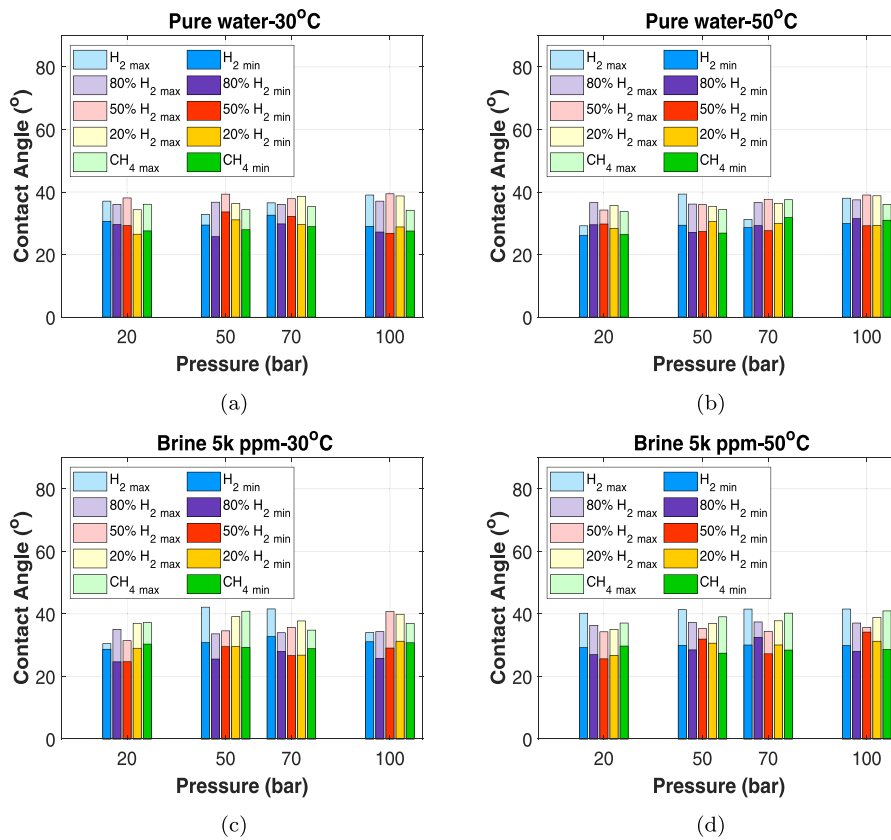

Fig. 3. Contact angle results for all 5 different gas compositions as a function of pressure and for 2 different temperatures of 30°C and 50°C, pure water (a, b) and brine 5000 ppm NaCl (c, d) in contact with Bentheimer sandstone. The results for pure H_2 are based on the experimental observations of Hashemi et al. (2021b).

Here θ [°] is the contact angle and s [m] is the distance along the surface contour, as illustrated in Fig. 1. By replacing R_1 and R_2 in Eq. (6) with Eqs. (7) and (8), respectively, one obtains

$$\frac{d\theta}{ds} = \frac{2}{b} + \frac{\Delta \rho g z}{\sigma} - \frac{\sin \theta}{x}. \tag{9}$$

Eq. (9) can be stated in dimensionless form as

$$\frac{d\theta}{ds^*} = \frac{2}{b^*} + \frac{\Delta \rho g R^2}{\sigma} z^* - \frac{\sin \theta}{x^*}, \tag{10}$$

where the bubble radius R is used as characteristic length scale, i.e., $x^* = x/R$. The second term on the right hand side of Eq. (9) is

the Bond number (N_{Bo}), defined as

$$N_{Bo} = \frac{\Delta \rho g R^2}{\sigma}. \tag{11}$$

N_{Bo} is the ratio of gravitational forces to interfacial forces (Alvarez et al., 2009; Hessel et al., 2004; Berg, 2010).

3. Results and discussion

Contact angles for H_2–CH_4/brine/rock systems were measured using the captive bubble cell method. Although this method does not take into account the impact of pore structures and flow dynamics on the wettability, it sheds lights on the wettability behaviour in
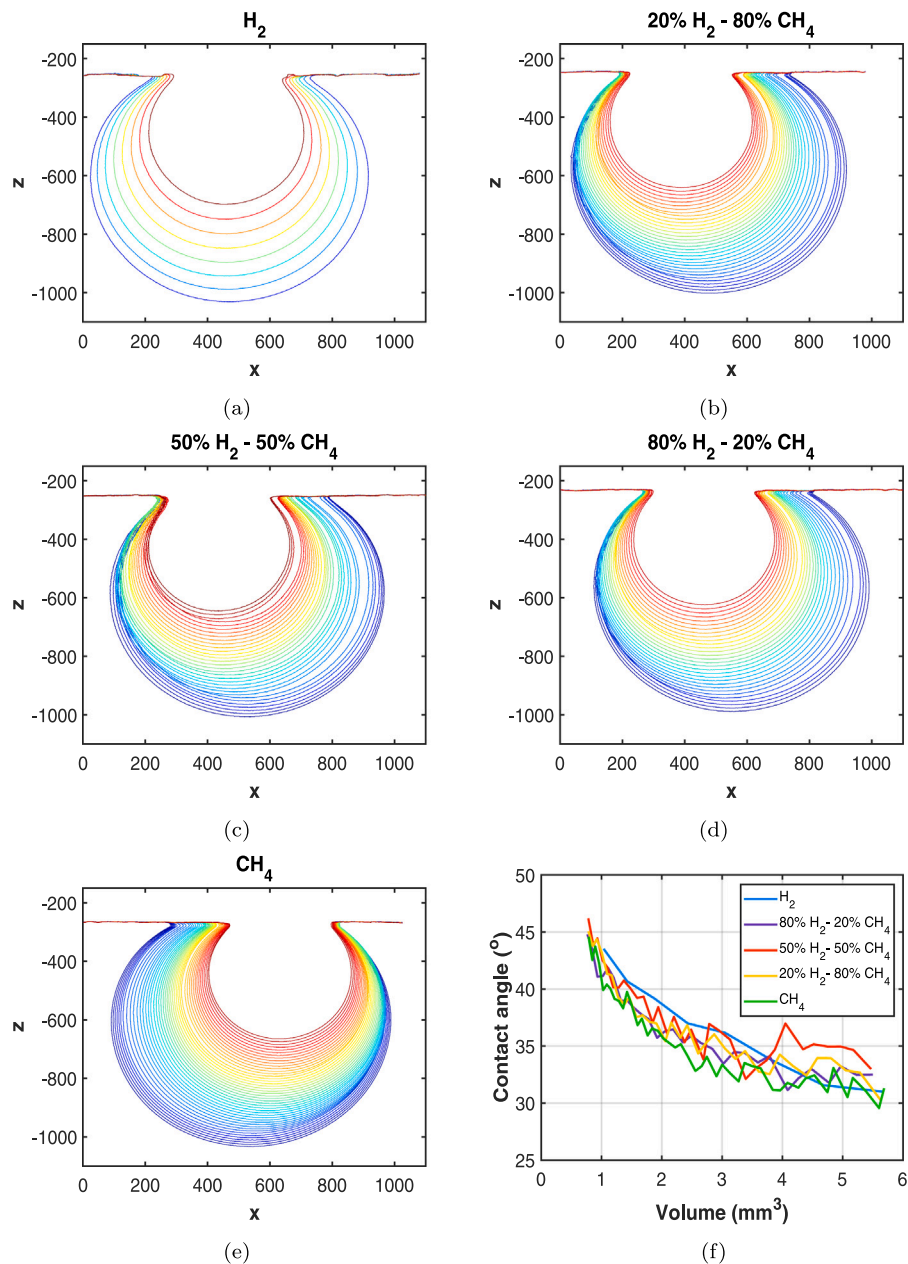
Fig. 4. Bubble contours over time for 5 different gas compositions and pure water in contact with Bentheimer sandstone, at 30 °C and 100 bar, and their contact angles versus bubble volumes (f).

systems where buoyancy and capillary are the main driving forces. Furthermore, it provides insights on the overall wettability state of sandstone rock in contact with gas mixtures of H_2–CH_4 and brine. The experiments were carried out for a range of pressures, two temperatures and two different brine salinities, the results of which can be seen in Fig. 3 and Tables B.1–B.11 of Appendix B. The results for pure H_2 are based on the experimental observations of Hashemi et al. (2021b) who used the same captive-bubble cell device to measure contact angles for the H_2/Brine/Bentheimer system. In addition, in Fig. 6 the contact angles for pure H_2 measured on a third Bentheimer sandstone sample are presented to highlight the systematic change in contact angle that is observed when different samples are used. All Bentheimer sandstone samples used in this study were cut from the same Bentheimer sandstone block. To verify whether changes in the chemical composition or rock structure occurred over time and consequently changed the contact angle, experiments were repeated. Fig. 2(a) shows the contact angle for different bubble sizes for three hydrogen experiments carried

out on the same rock slab. Between each of the experiments the rock slab was taken out of the apparatus and put in the vacuum oven to dry. It can be seen that similar results were obtained for each of these experiments. This indicates that no mineral alteration or other changes in the structure of the rock surface has taken place that significantly impacted the wettability.

The bubble size decreased with time, which is likely due to dissolution and diffusion into the brine. To verify whether dissolution into the brine would have an impact on the contact angle measurement, experiments were carried out using brine with different levels of hydrogen saturation. Fig. 2(a) shows the contact angle versus volume while Fig. 2(b) shows the contact angle versus time for a system where the brine was highly saturated with hydrogen and a system where the brine was unsaturated. It can be seen that the dissolution rate of the unsaturated brine is almost 10 times higher than the (highly) saturated brine. However, the contact angles obtained are the same in each of the experiments. This shows that the contact angle is a function of

the bubble size and does not depend on the saturation level. Using unsaturated brine allowed us to make contact angle measurements for a range of bubble sizes. It is observed that the contact angle increases with decreasing bubble size. The minimum and maximum contact angle values in Fig. 3 correspond to the largest and smallest bubble sizes.

3.1. Effect of bubble size and gas composition

The gas bubbles were released in under-saturated brine solutions and slowly dissolved and diffused into the brine. Images were taken every minute, except for pure H_2, where the time-step between images was four minutes. For each of these images the contour of the interface was detected and contact angles were calculated. Fig. 4 shows the contours of the interfaces at each time-step as well as the corresponding bubble volume and contact angle for three H_2–CH_4 mixtures, pure H_2 and pure CH_4, for a system with pure water at 30 °C and 100 bar. Due to the roughness of the sample pinning of the gas bubble occurred and as a result the dissolution was not symmetric. In some cases this pinning led to higher contact angles as can be observed in Fig. 4(e) for 50% H_2–CH_4 mixture for bubbles bigger than 4 mm³. Overall, the gas bubbles of the different mixtures show comparable behaviour. Although, the contact angles of the H_2 bubbles are slightly higher. This is likely due to the fact that a different Bentheimer sandstone sample, although obtained from the same block, was used for the H_2 experiments, since the contact angles of the different mixture compositions are indistinguishable. The contact angle is a function of the bubble volume and no distinction can be made between the different gases. This behaviour of increasing contact angle with decreasing bubble volume has also previously been reported for CO_2/brine/rock systems (Kaveh et al., 2014; Drelich, 1997; Haeri et al., 2020; Jung and Wan, 2012).

3.2. Effect of pressure, temperature and salinities

For all experimental conditions water-wet behaviour was observed with contact angles ranging between [25°–45°] for all H_2–CH_4 mixtures as well as for pure H_2 and pure CH_4 as can be seen in Fig. 3. No obvious correlation between the measured contact angle and the pressures, temperatures or salinity could be observed. Note that the range of bubble sizes was different for the different experiments. High contact angle values correspond to smaller bubble sizes. However, for similar bubble sizes all the data points fall within the accuracy range of the conducted experiments (± 3°). To validate our findings a sensitivity study of the captive-bubble cell approach to measure wettability, based on the Young–Laplace equation, has been performed. This is presented in the following section.

3.3. Sensitivity analysis of the captive-bubble cell approach

The contact angles presented in this study were obtained by fitting Eq. (9) onto the captured images of the gas bubbles. A closer look at Eq. (9) shows that three parameters impact the fitting curve formula: apex radius (b), density difference ($\Delta\rho$) and interfacial tension (σ), of which the combined impact can be characterized by the Bond number, as defined in Eq. (11). To investigate the impact of each of these three parameters on the contact angle, a systematic sensitivity analysis has been performed, the results of which can be seen in Fig. 5.

Based on the experimental observations, the ratio of the surface position to the height h,(see Fig. 1) is changing from 0.8 to 0.95, corresponding to the biggest and smallest bubble sizes, respectively. Therefore as the base-case, σ was set to 60 mN/m, $\Delta\rho$ to 1000 kg/m³, b to 1 mm and the surface location, z, was set to 0.9 of the bubble height. It is important to note that the ratio of the surface position to the height h depends on the wetting state of the system.

Fig. 5a shows the results of the analysis for the apex radius effect. It can be seen that the contact angle increases with decreasing apex radius, in a similar fashion as was observed from the experiments.
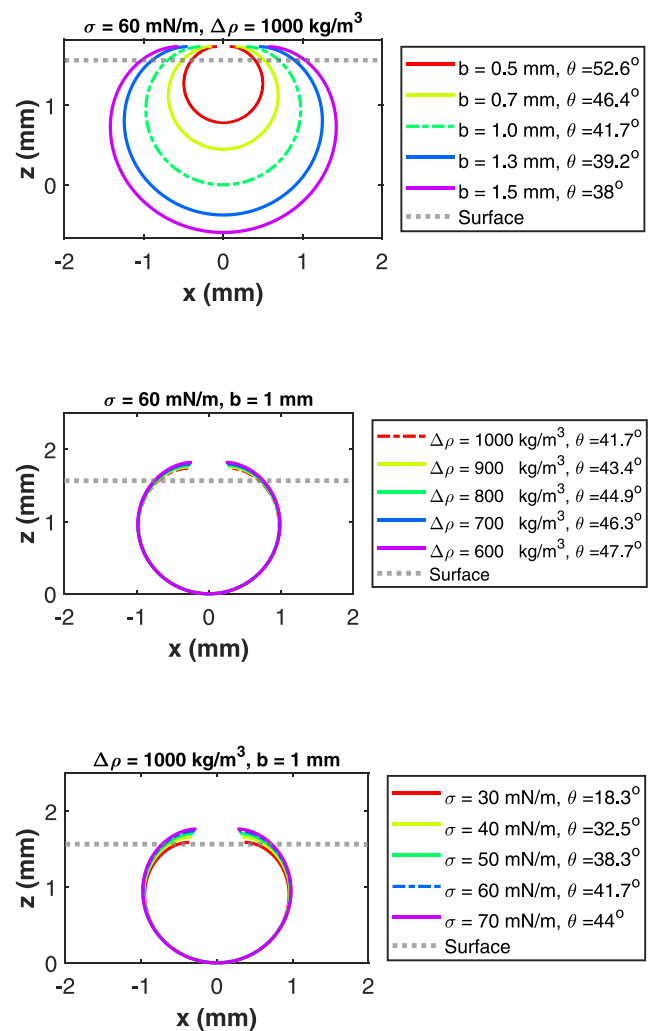
Fig. 5. Sensitivity analysis for captive-bubble method for wettability characterization: effect of apex radius (top), density difference (middle) and interfacial tension (bottom) on the contact angle.

The effect of the density contrast on the contact angle is presented in Fig. 5b. Here, the contact angle increases with decreasing $\Delta\rho$. However, for the $\Delta\rho$ of this study, which is in the range of 900–1000 kg/m³ the contact angle ranges between [41.7–43.4]°, which is within the accuracy range of the measuring technique. Fig. 5c shows the effect of interfacial tension on the contact angle. It can be seen that the contact angle increases with increasing interfacial tension. For the pressures and temperatures of our study, the interfacial tensions of the different H_2–CH_4 mixtures likely ranged between [50–70] mN/m (Hassanpouryouzband et al., 2021; Chow et al., 2018; Pan et al., 2020). In this range, the contact angle varies between [38.3°–44°]. For a particular set of conditions, this is again within the accuracy range of the measuring technique. The above analysis shows that no significant pressure, temperature and salinity dependency is expected in systems where buoyancy and capillarity are the main driving forces such as our captive bubble cell, which validates our results. However in different systems where other driving forces come into play, including different experimental measurement techniques, these factors could have a bigger impact on the contact angle, as has been observed in literature.

The Bond number for the H_2/water and CH_4/water experiments are plotted in Fig. 6a, as a function of radius at the apex point. It can be seen that the Bond numbers of both the H_2/water and CH_4/water systems are comparable, and depend on the size of the bubble. Fig. 6b
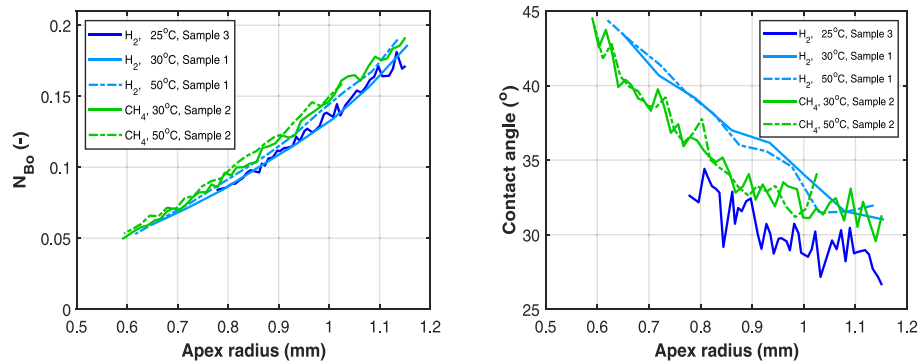
Fig. 6. Bond number (left) and contact angle measurements (right) for H$_2$ and CH$_4$ versus different apex radii corresponding to the bubble size changes over time, at the fixed pressure of 100 bar and temperatures of 30°C and 50°C. The slight difference between the contact angles of H$_2$ and CH$_4$ is due to the fact that different samples were used, because Fig. 4 (bottom right) shows that for the same samples the contact angles match.
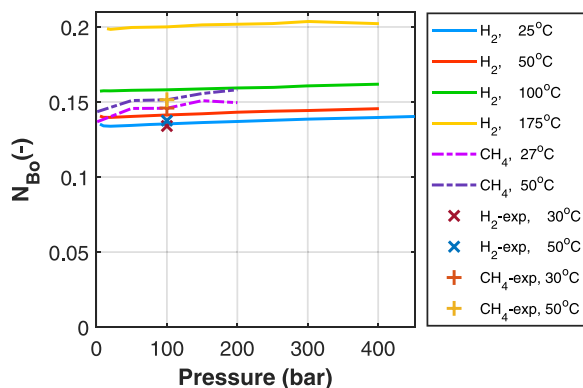

Fig. 7. Theoretically calculated Bond number based on the IFT (Chow et al., 2018) and density (Pan et al., 2020) values of H$_2$ and CH$_4$ from the literature. Calculations are made for the constant apex radius of 1 mm. The x and + markers indicate the Bond numbers corresponding to Fig. 6 with the apex radius of 1 mm.

shows that under similar Bond numbers and similar bubble sizes, the contact angles of H$_2$ and CH$_4$ bubbles and their mixtures are indeed comparable. The slight difference between the contact angle plots is due to the fact that different Bentheimer sandstone samples were used.

The experiments of this study were carried out for pressures ranging between [20–100] bar and temperatures between [20–50] °C. Bond numbers for much higher pressures [0–450] bar and temperatures [25–175] °C were also calculated and plotted in Fig. 7, using the literature values for σ and $\Delta\rho$. It can be seen that the Bond number stays relatively constant through the entire studied range, and only a small increase with temperature is observed. This analysis shows that the Bond numbers of H$_2$ and CH$_4$ are indeed comparable, even for this wide range of conditions. This indicates that in real field processes in which buoyancy and capillary are the main acting forces, H$_2$, CH$_4$ and their mixture in contact with brine, will have similar wettability characteristics independent of pressure and temperature.

4. Conclusions

In this study static contact angles for H$_2$–CH$_4$ mixtures, pure H$_2$ and pure CH$_4$ in contact with brine and Bentheimer sandstone rock were measured using the captive-bubble cell device for a range of pressures (20–100 bar), two temperatures (30°, 50°), and two salinities (pure water, 5000 ppm). Strongly water-wet conditions were observed with contact angles ranging between [25°–45°] for all CH$_4$–H$_2$ mixtures. All of the gas mixtures showed comparable behaviour and no pressure, temperature or salinity dependency was observed. The size of the injected gas bubbles decreased with time due to dissolution and diffusion

into the brine, which allowed for static contact angle measurements for various bubble sizes. Our analysis showed that contact angles increased with decreasing bubble volume.

For the static system, the acting buoyancy and surface forces allow for analytical sensitivity analysis for the captive bubble cell approach, which is based on the Young–Laplace equation, to characterize the wettability. Three parameters in the Young Laplace equation affect the contact angle: radius at the apex, density difference, and interfacial tension. The sensitivity analysis showed an increase in contact angle for a decrease in radius at the apex similar to what was observed in the experiments. Furthermore, for the range of interfacial tensions and density differences that correspond to the experimental conditions of this study, the analysis showed that the changes in contact angle are such that they fall within the accuracy range of the experiment validating our results.

It is mathematically shown that for comparable bubble sizes and under similar Bond numbers the contact angles of hydrogen and methane bubbles and their mixtures in contact with brine will indeed be comparable. This indicates that for real field processes in which buoyancy and capillary are the main acting forces, hydrogen, methane and their mixture will have similar wettability characteristics.

CRediT authorship contribution statement

Declaration of competing interest

The authors declare that they have no known competing financial interests or personal relationships that could have appeared to influence the work reported in this paper.
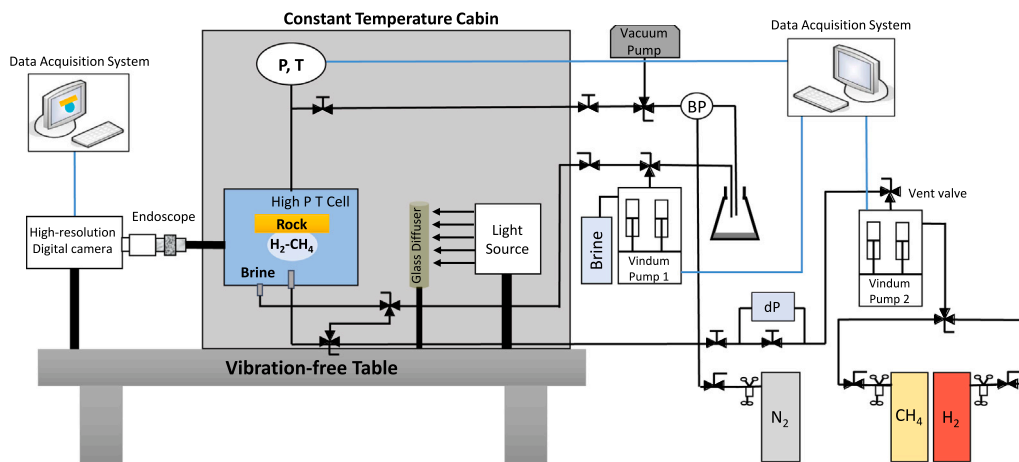
Acknowledgements

Fig. A.1. Schematic of the captive-bubble cell device used for the experiments.

Table B.1
Contact angle values of H_2/pure water/Bentheimer (Hashemi et al., 2021b).

Test No.	Temp. (°C)	Press. (bar)	ϑ_{ave} (°)	ϑ_{range} (°)	Vol.$_{ave}$ (mm³)	Vol.$_{range}$ (mm³)
T~30 °C	31.9	22	33.7	[30.6, 37.1]	3.48	[2.21, 4.66]
	32.5	51.8	30.5	[29.4, 32.9]	3.09	[2.20, 3.66]
	32.8	71.5	33.9	[32.6, 36.5]	3.39	[2.38, 4.48]
	33.2	100.5	31.7	[29.0, 39.0]	5.27	[1.93, 9.49]
T~50 °C	49.1	19.8	28.4	[26.1, 29.2]	7.42	[3.96, 10.65]
	49.2	50.6	33.2	[29.4, 39.3]	4.7	[1.68, 8.39]
	49.3	70.2	29.8	[28.6, 31.2]	4.41	[2.66, 6.33]
	49.3	101.2	32.8	[29.9, 38.0]	4.12	[2.14, 6.35]

Table B.2
Contact angle values of H_2/brine (5000 ppm NaCl)/Bentheimer (Hashemi et al., 2021b).

Test No.	Temp. (°C)	Press. (bar)	ϑ_{ave} (°)	ϑ_{range} (°)	Vol.$_{ave}$ (mm³)	Vol.$_{range}$ (mm³)
T~30 °C	31.7	21	29.5	[28.7, 30.5]	4.61	[2.67, 6.55]
	32.2	49.9	34.9	[30.8, 42.2]	3.42	[1.21, 5.77]
	32.7	71.1	36	[32.8, 41.6]	2.8	[1.19, 4.72]
	33.1	98.9	31.9	[31.1, 34.1]	5.59	[2.08, 11.13]
T~50 °C	47.4	20.7	33.6	[29.2, 40.2]	4.48	[1.51, 7.78]
	48.3	51.3	33.6	[29.9, 41.4]	4.03	[1.40, 6.45]
	49	70.6	34.2	[30.0, 41.5]	4.34	[1.50, 7.91]
	49.2	100.7	33.7	[29.9, 41.6]	5.7	[1.31, 12.66]

Table B.3
Contact angle values of (80% H_2–20% CH_4)/pure water/Bentheimer.

Test No.	Temp. (°C)	Press. (bar)	ϑ_{ave} (°)	ϑ_{range} (°)	Vol.$_{ave}$ (mm³)	Vol.$_{range}$ (mm³)
T~30 °C	32.1	21.1	32.6	[29.6, 36.0]	6.20	[2.27,11.23]
	32.1	49.0	31.8	[25.7, 36.7]	6.40	[2.44,10.77]
	32.1	68.4	32.9	[29.8, 36.1]	6.20	[2.02,12.17]
	32.1	100.8	33.2	[27.2, 37.1]	6.03	[2.32,10.72]
T~50 °C	48.2	22.2	32.7	[29.5, 36.6]	6.10	[2.36,11.33]
	48.3	49.5	32.2	[27.1, 36.1]	6.31	[1.99,11.20]
	48.4	70.3	32.4	[29.2, 36.6]	6.42	[2.14,11.74]
	48.4	99.9	33.3	[31.5, 37.5]	6.89	[1.97,13.25]

Appendix A. Experimental apparatus and procedure

A schematic of the experimental apparatus can be seen in Fig. A.1.

Appendix B. Contact angle measurements

In the following, the contact angles for the gas/brine/Bentheimer systems, measured directly from the images, at different pressure, temperature and salinity values are listed (Tables B.1–B.11). For completeness the contact angles for H_2 which were presented in Hashemi et al. (2021b) are included as well. In addition, the density values used in the calculation of the contact angles can be found in Tables B.12–B.22. The densities of the mixtures were calculated based on the pure gas densities according to

$$\rho_m = (\rho_1 V_1 + \rho_2 V_2)/(V_1 + V_2). \tag{B.1}$$

Here, ρ is density [kg/m³], V is volume [m³] and subscripts m, 1, 2 stand for mixture, gas 1 and gas 2, respectively. This can conveniently be calculated using the website www.fluidat.com.

Table B.4
Contact angle values of (80% H$_2$–20% CH$_4$)/brine (5000 ppm NaCl)/Bentheimer.

Test No.	Temp. (°C)	Press. (bar)	ϑ_{ave} (°)	ϑ_{range} (°)	Vol.$_{ave}$ (mm^3)	Vol.$_{range}$ (mm^3)
T~30 °C	33.1	19.7	30.0	[24.7,35.1]	6.47	[2.00,12.18]
	32.8	50.1	30.3	[25.6,33.6]	6.10	[2.32,12.13]
	32.8	71.3	30.3	[27.9,33.9]	6.72	[2.78,11.72]
	32.7	99.4	30.4	[25.8,34.3]	6.58	[2.36,12.64]
T~50 °C	48.9	21.3	31.6	[26.9,36.3]	6.62	[2.38,10.78]
	49.0	49.4	32.3	[28.5,37.3]	7.03	[2.81,12.21]
	49.0	70.8	34.6	[32.5,37.4]	4.47	[2.61,6.02]
	49.1	99.0	32.5	[28.0,37.1]	5.61	[2.29,8.72]

Table B.5
Contact angle values of (50% H$_2$–50% CH$_4$)/pure water/Bentheimer.

Test No.	Temp. (°C)	Press. (bar)	ϑ_{ave} (°)	ϑ_{range} (°)	Vol.$_{ave}$ (mm^3)	Vol.$_{range}$ (mm^3)
T~30 °C	31.8	20.7	32.7	[29.2,38.1]	5.72	[2.05,9.93]
	31.9	46.7	35.7	[33.6,39.3]	3.86	[1.61,6.52]
	32.0	68.2	34.5	[32.2,37.8]	4.54	[1.94,6.79]
	32.0	104.2	33.4	[26.8,39.4]	5.74	[1.71,11.59]
T~50 °C	47.7	21.3	32.1	[29.8,34.2]	5.39	[2.44,8.22]
	47.7	52.2	32.4	[27.3,35.9]	3.72	[1.76,5.59]
	47.7	69.6	33.2	[27.6,37.7]	5.98	[2.22,10.59]
	47.7	98.3	32.9	[29.2,39.0]	3.72	[1.71,6.27]

Table B.6
Contact angle values of (50% H$_2$–50% CH$_4$)/brine (5000 ppm NaCl)/Bentheimer.

Test No.	Temp. (°C)	Press. (bar)	ϑ_{ave} (°)	ϑ_{range} (°)	Vol.$_{ave}$ (mm^3)	Vol.$_{range}$ (mm^3)
T~30 °C	32.1	20.9	27.2	[24.7,31.4]	6.71	[3.28,10.78]
	32.2	49.2	31.4	[29.5,34.6]	5.47	[2.43,9.06]
	32.2	71.3	31.9	[26.6,35.7]	6.17	[2.13,10.70]
	32.3	100.5	35.0	[29.1,40.8]	4.52	[1.48,9.13]
T~50 °C	48.2	20.2	29.9	[25.6,34.3]	6.04	[2.61,9.93]
	48.2	50.5	33.9	[31.9,35.3]	3.26	[2.24,4.43]
	48.0	70.5	30.1	[27.2,34.4]	5.08	[2.26,8.48]
	48.0	100.7	34.6	[34.2,35.7]	5.20	[3.67,6.88]

Table B.7
Contact angle values of (20% H$_2$–80% CH$_4$)/pure water/Bentheimer.

Test No.	Temp. (°C)	Press. (bar)	ϑ_{ave} (°)	ϑ_{range} (°)	Vol.$_{ave}$ (mm^3)	Vol.$_{range}$ (mm^3)
T~30 °C	32.1	21.0	31.4	[26.5,34.3]	6.82	[2.92,12.16]
	32.1	51.1	33.7	[31.1,36.3]	4.88	[2.21,8.31]
	32.0	68.6	32.8	[29.6,38.6]	6.10	[1.74,11.61]
	32.1	101.4	34.7	[28.8,38.7]	3.42	[1.57,6.20]
T~50 °C	47.9	21.0	31.6	[28.3,35.7]	6.24	[2.51,10.78]
	48.2	49.9	32.9	[30.5,35.4]	4.23	[2.26,6.47]
	48.4	69.3	33.5	[29.9,36.4]	4.56	[2.09,8.16]
	48.6	102.9	34.3	[29.3,38.8]	4.82	[1.44,10.01]

Table B.8
Contact angle values of (20% H$_2$–80% CH$_4$)/brine (5000 ppm NaCl)/Bentheimer.

Test No.	Temp. (°C)	Press. (bar)	ϑ_{ave} (°)	ϑ_{range} (°)	Vol.$_{ave}$ (mm^3)	Vol.$_{range}$ (mm^3)
T~30 °C	31.8	20.6	32.4	[29.0,37.0]	6.25	[2.11,10.92]
	31.9	48.8	33.5	[29.6,39.1]	5.86	[1.59,11.42]
	32.0	70.8	32.5	[26.8,37.7]	5.91	[1.97,11.52]
	32.1	102.0	35.2	[31.3,39.9]	3.53	[1.31,6.29]
T~50 °C	47.3	19.1	31.9	[26.7,35.0]	6.53	[2.41,11.73]
	47.9	48.8	33.3	[30.6,36.9]	3.95	[2.07,5.65]
	48.5	70.5	34.5	[30.1,37.8]	5.10	[2.92,7.37]
	49.0	102.2	34.5	[31.3,38.9]	4.28	[1.78,7.32]

Table B.9
Contact angle values of CH_4/pure water/Bentheimer.

Test No.	Temp. (°C)	Press. (bar)	ϑ_{ave} (°)	ϑ_{range} (°)	Vol.$_{ave}$ (mm^3)	Vol.$_{range}$ (mm^3)
T~30 °C	31.6	21.1	31.8	[27.5,36.1]	6.08	[2.08,10.99]
	31.8	47.4	31.2	[27.9,34.3]	4.77	[2.32,8.08]
	31.9	70.0	32.6	[28.9,35.3]	5.61	[2.14,8.70]
	32.1	99.1	31.7	[27.5,34.2]	4.97	[2.34,7.61]
T~50 °C	48.1	20.5	30.0	[26.4,33.7]	7.37	[2.29,13.21]
	48.2	49.4	30.6	[26.9,34.4]	6.17	[2.73,10.35]
	48.3	70.9	33.8	[31.8,37.5]	2.63	[1.57,3.85]
	48.2	100.0	33.5	[30.9,36.1]	3.05	[1.85,4.52]

Table B.10
Contact angle values of CH_4/brine (5000 ppm NaCl)/Bentheimer.

Test No.	Temp. (°C)	Press. (bar)	ϑ_{ave} (°)	ϑ_{range} (°)	Vol.$_{ave}$ (mm^3)	Vol.$_{range}$ (mm^3)
T~30 °C	32.1	20.7	33.8	[30.3,37.3]	4.66	[3.56,6.33]
	32.3	49.0	34.1	[29.3,40.8]	5.75	[2.02,10.26]
	32.5	69.7	32.6	[28.8,34.8]	4.67	[2.80,6.74]
	32.7	100.1	34.6	[30.7,36.9]	5.87	[2.02,9.29]
T~50 °C	47.9	21.6	33.5	[29.7,37.1]	5.67	[2.95,9.78]
	48.1	49.5	33.9	[27.4,39.1]	5.75	[1.88,11.48]
	48.2	71.7	34.8	[28.4,40.2]	5.06	[1.53,10.42]
	48.3	98.7	35.6	[28.6,40.9]	3.71	[1.73,6.14]

Table B.11
Contact angle values of CH_4/brine (50000 ppm NaCl)/Bentheimer.

Test No.	Temp. (°C)	Press. (bar)	ϑ_{ave} (°)	ϑ_{range} (°)	Vol.$_{ave}$ (mm^3)	Vol.$_{range}$ (mm^3)
T~30 °C	32.2	20.3	36.0	[35.0,36.3]	4.57	[3.52,5.63]
	32.3	50.0	33.3	[28.9,37.9]	5.59	[3.38,8.01]
	32.4	73.5	34.9	[31.3,38.9]	3.55	[2.16,5.26]
	32.6	100.4	33.9	[29.5,38.5]	3.66	[2.15,5.32]
T~50 °C	48.4	18.0	29.2	[26.6,31.3]	6.42	[5.60,7.34]
	48.6	49.6	32.6	[25.1,38.5]	7.29	[4.64,10.48]
	48.6	71.1	35.2	[29.4,40.4]	3.99	[1.82,6.53]
	48.8	99.7	36.0	[28.9,41.8]	6.31	[4.11,9.31]

Table B.12
Density of liquid and gas phases used for contact angle measurement of H_2/pure water/Bentheimer tests (Hashemi et al., 2021b).

Temp. (°C)	Press. (bar)	ρ_{liquid}(kg/m^3)	ρ_{gas}(kg/m^3)
31.9	22.0	995.12	1.73
32.5	51.8	996.25	3.99
32.8	71.5	997.01	5.44
33.2	100.5	998.15	7.51
49.1	19.8	989.17	1.47
49.2	50.6	990.44	3.70
49.3	70.2	991.23	5.08
49.3	101.2	992.53	7.20

Table B.14
Density of liquid and gas phases used for contact angle measurement of (80% H_2–20% CH_4)/pure water/Bentheimer tests.

Temp. (°C)	Press. (bar)	ρ_{liquid}(kg/m^3)	ρ_{gas}(kg/m^3)
32.1	21.1	995.02	3.98
32.1	49.0	996.24	9.15
32.1	68.4	997.09	12.66
32.1	100.8	998.49	18.34
48.2	22.2	989.62	3.98
48.3	49.5	990.74	8.77
48.4	70.3	991.59	12.34
48.4	99.9	992.83	17.27

Table B.13
Density of liquid and gas phases used for contact angle measurement of H_2/brine (5000 ppm NaCl)/Bentheimer tests (Hashemi et al., 2021b).

Temp. (°C)	Press. (bar)	ρ_{liquid}(kg/m^3)	ρ_{gas}(kg/m^3)
31.7	21.0	998.24	1.65
32.2	49.9	999.36	3.85
32.7	71.1	1000.13	5.41
33.1	98.9	1001.21	7.40
47.4	20.7	992.88	1.55
48.3	51.3	993.82	3.76
49.0	70.6	994.35	5.11
49.2	100.7	995.53	7.16

Table B.15
Density of liquid and gas phases used for contact angle measurement of (80% H_2–20% CH_4)/brine (5000 ppm NaCl)/Bentheimer tests.

Temp. (°C)	Press. (bar)	ρ_{liquid}(kg/m^3)	ρ_{gas}(kg/m^3)
33.1	19.7	997.77	3.71
32.8	50.1	999.19	9.33
32.8	71.3	1000.11	13.14
32.7	99.4	1001.36	18.07
48.9	21.3	992.31	3.81
49.0	49.4	993.46	8.74
49.0	70.8	994.36	12.40
49.1	99.0	995.50	17.09

Table B.16

Density of liquid and gas phases used for contact angle measurement of (50% H_2–50% CH_4)/pure water/Bentheimer tests.

Temp. (°C)	Press. (bar)	ρ_{liquid}(kg/m^3)	ρ_{gas}(kg/m^3)
31.8	20.7	995.09	7.49
31.9	46.7	996.20	17.25
32.0	68.2	997.11	25.53
32.0	104.2	998.67	39.68
47.7	21.3	989.78	7.31
47.7	52.2	991.09	18.22
47.7	69.6	991.83	24.48
47.7	98.3	993.04	34.88

Table B.17

Density of liquid and gas phases used for contact angle measurement of (50% H_2–50% CH_4)/brine (5000 ppm NaCl)/Bentheimer tests.

Temp. (°C)	Press. (bar)	ρ_{liquid}(kg/m^3)	ρ_{gas}(kg/m^3)
32.1	20.9	998.12	7.56
32.2	49.2	999.33	18.18
32.2	71.3	1000.29	26.26
32.3	100.5	1001.53	36.74
48.2	20.2	992.54	6.92
48.2	50.5	993.82	17.58
48	70.5	994.75	24.77
48	100.7	996.01	35.70

Table B.18

Density of liquid and gas phases used for contact angle measurement of (20% H_2–80% CH_4)/pure water/Bentheimer tests.

Temp. (°C)	Press. (bar)	ρ_{liquid}(kg/m^3)	ρ_{gas}(kg/m^3)
32.1	21.0	995.01	11.13
32.1	51.1	996.33	27.63
32.0	68.6	997.12	37.43
32.1	101.4	998.52	55.93
47.9	21.0	989.69	10.55
48.2	49.9	990.80	25.39
48.4	69.3	991.54	35.48
48.6	102.9	992.88	52.98

Table B.19

Density of liquid and gas phases used for contact angle measurement of (20% H_2–80% CH_4)/brine (5000 ppm NaCl)/Bentheimer tests.

Temp. (°C)	Press. (bar)	ρ_{liquid}(kg/m^3)	ρ_{gas}(kg/m^3)
31.8	20.6	998.20	10.93
31.9	48.8	999.40	26.37
32.0	70.8	1000.33	38.67
32.1	102.0	1001.65	56.26
47.3	19.1	992.85	9.61
47.9	48.8	993.87	24.85
48.5	70.5	994.55	36.09
49.0	102.2	995.68	52.54

Table B.20

Density of liquid and gas phases used for contact angle measurement of CH_4/pure water/Bentheimer tests.

Temp. (°C)	Press. (bar)	ρ_{liquid}(kg/m^3)	ρ_{gas}(kg/m^3)
31.6	21.1	995.16	13.81
31.8	47.4	996.26	32.26
31.9	70.0	997.21	49.18
32.1	99.1	998.42	72.04
48.1	20.5	989.59	12.63
48.2	49.4	990.78	31.50
48.3	70.9	991.65	46.25
48.2	100.0	992.91	66.97

Table B.21

Density of liquid and gas phases used for contact angle measurement of CH_4/brine (5000 ppm NaCl)/Bentheimer tests.

Temp. (°C)	Press. (bar)	ρ_{liquid}(kg/m^3)	ρ_{gas}(kg/m^3)
32.1	20.7	998.11	13.51
32.3	49.0	999.29	33.35
32.5	69.7	1000.13	48.80
32.7	100.1	1001.39	72.61
47.9	21.6	989.71	13.34
48.1	49.5	990.82	31.58
48.2	71.7	991.72	46.83
48.3	98.7	992.82	66.00

Table B.22

Density of liquid and gas phases used for contact angle measurement of CH_4/brine (50000 ppm NaCl)/Bentheimer tests.

Temp. (°C)	Press. (bar)	ρ_{liquid}(kg/m^3)	ρ_{gas}(kg/m^3)
32.2	20.3	1003.16	13.24
32.3	50.0	1004.32	34.11
32.4	73.5	1005.22	51.75
32.6	100.4	1006.14	72.89
48.4	18.0	992.37	11.05
48.6	49.6	993.63	31.59
48.6	71.1	994.53	46.33
48.8	99.7	995.65	66.56

References

Alhammadi, A.M., AlRatrout, A., Singh, K., Bijeljic, B., Blunt, M.J., 2017. In situ characterization of mixed-wettability in a reservoir rock at subsurface conditions. Sci. Rep. 7 (1), 1–9.

Ali, M., Yekeen, N., Pal, N., Keshavarz, A., Iglauer, S., Hoteit, H., 2021. Influence of pressure, temperature and organic surface concentration on hydrogen wettability of caprock; implications for hydrogen geo-storage. Energy Rep. 7, 5988–5996. http://dx.doi.org/10.1016/j.egyr.2021.09.016, URL: https://www.sciencedirect.com/science/article/pii/S2352484721008210.

Alvarez, N.J., Walker, L.M., Anna, S.L., 2009. A non-gradient based algorithm for the determination of surface tension from a pendant drop: Application to low bond number drop shapes. J. Colloid Interface Sci. 333 (2), 557–562. http://dx.doi.org/10.1016/j.jcis.2009.01.074, URL: https://www.sciencedirect.com/science/article/pii/S0021979709002161.

Arif, M., Abu-Khamsin, S.A., Iglauer, S., 2019. Wettability of rock/CO2/brine and rock/oil/CO2-enriched-brine systems: Critical parametric analysis and future outlook. Adv. Colloid Interface Sci. 268, 91–113.

Berg, J.C., 2010. An Introduction to Interfaces & Colloids: The Bridge to Nanoscience. World Scientific.

Carden, P., Paterson, L., 1979. Physical, chemical and energy aspects of underground hydrogen storage. Int. J. Hydrogen Energy 4 (6), 559–569. http://dx.doi.org/10.1016/0360-3199(79)90083-1.

Chow, Y.F., Maitland, G.C., Trusler, J.M., 2018. Interfacial tensions of (H2O+ H2) and (H2O+ CO2+ H2) systems at temperatures of (298–448) K and pressures up to 45 MPa. Fluid Phase Equilib. 475, 37–44.

De Gennes, P.-G., 1985. Wetting: statics and dynamics. Rev. Modern Phys. 57 (3), 827.

Drelich, J., 1997. The effect of drop (bubble) size on contact angle at solid surfaces. J. Adhes. 63 (1–3), 31–51. http://dx.doi.org/10.1080/00218469708015212.

Gabrielli, P., Poluzzi, A., Kramer, G.J., Spiers, C., Mazzotti, M., Gazzani, M., 2020. Seasonal energy storage for zero-emissions multi-energy systems via underground hydrogen storage. Renew. Sustain. Energy Rev. 121, 109629. http://dx.doi.org/10.1016/j.rser.2019.109629, URL: http://www.sciencedirect.com/science/article/pii/S1364032119308366.

Haeri, F., Tapriyal, D., Sanguinito, S., Shi, F., Fuchs, S.J., Dalton, L.E., Baltrus, J., Howard, B., Crandall, D., Matranga, C., Goodman, A., 2020. CO2–brine contact angle measurements on Navajo, Nugget, Bentheimer, Bandera Brown, Berea, and Mt. Simon Sandstones. In: Energy & Fuels. Energy Fuels 34 (5), 6085–6100. http://dx.doi.org/10.1021/acs.energyfuels.0c00436.

Hashemi, L., Blunt, M., Hajibeygi, H., 2021a. Pore-scale modelling and sensitivity analyses of hydrogen-brine multiphase flow in geological porous media. Sci. Rep. 11 (1), 8348. http://dx.doi.org/10.1038/s41598-021-87490-7.

Hashemi, L., Glerum, W., Farajzadeh, R., Hajibeygi, H., 2021b. Contact angle measurement for hydrogen/brine/sandstone system using captive-bubble method relevant for underground hydrogen storage. Adv. Water Resour. 103964.

Hassanpouryouzband, A., Joonaki, E., Edlmann, K., Haszeldine, R.S., 2021. Offshore geological storage of hydrogen: Is this our best option to achieve net-zero? ACS Energy Lett. 6 (6), 2181–2186.

Hassanpouryouzband, A., Joonaki, E., Edlmann, K., Heinemann, N., Yang, J., 2020. Thermodynamic and transport properties of hydrogen containing streams. Sci. Data 7 (1), 1–14.

Heinemann, N., Alcalde, J., Miocic, J.M., Hangx, S.J.T., Kallmeyer, J., Ostertag-Henning, C., Hassanpouryouzband, A., Thaysen, E.M., Strobel, G.J., Schmidt-Hattenberger, C., Edlmann, K., Wilkinson, M., Bentham, M., Stuart Haszeldine, R., Carbonell, R., Rudloff, A., 2021. Enabling large-scale hydrogen storage in porous media – the scientific challenges. Energy Environ. Sci. 14, 853–864. http://dx.doi.org/10.1039/D0EE03536J.

Hessel, V., Löwe, H., Hardt, S., 2004. Chemical Micro Process Engineering: Fundamentals, Modelling and Reactions. Vol. 1. John Wiley & Sons.

Higgs, S., Da Wang, Y., Sun, C., Ennis-King, J., Jackson, S., Armstrong, R., Mostaghimi, P., 2021. In-situ hydrogen wettability characterisation for underground hydrogen storage.

Iglauer, S., Ali, M., Keshavarz, A., 2021. Hydrogen wettability of sandstone reservoirs: Implications for hydrogen geo-storage. Geophys. Res. Lett. 48 (3), http://dx.doi.org/10.1029/2020GL090814, e2020GL090814.

Jung, J.-W., Wan, J., 2012. Supercritical CO2 and ionic strength effects on wettability of silica surfaces: Equilibrium contact angle measurements. In: Energy & Fuels. Energy Fuels 26 (9), 6053–6059. http://dx.doi.org/10.1021/ef300913t.

Kabuth, A., Dahmke, A., Beyer, C., Bilke, L., Dethlefsen, F., Dietrich, P., Duttmann, R., Ebert, M., Feeser, V., Görke, U.-J., et al., 2017. Energy storage in the geological subsurface: dimensioning, risk analysis and spatial planning: the ANGUS+ project. Environ. Earth Sci. 76 (1), 1–17.

Kaveh, N.S., Rudolph, E.S.J., van Hemert, P., Rossen, W.R., Wolf, K.H., 2014. Wettability evaluation of a CO2/water/bentheimer sandstone system: Contact angle, dissolution, and bubble size. In: Energy & Fuels. Energy Fuels 28 (6), 4002–4020. http://dx.doi.org/10.1021/ef500034j.

Kruck, O., Crotogino, F., Prelicz, R., Rudolph, T., 2013. Assessment of the Potential, the Actors and Relevant Business Cases for Large Scale and Seasonal Storage of Renewable Electricity by Hydrogen Underground Storage in Europe. KBB Undergr. Technol. GmbH.

Kunz, P., Hassanizadeh, S., Nieken, U., 2018. A two-phase SPH model for dynamic contact angles including fluid–solid interactions at the contact line. Transp. Porous Media 122 (2), 253–277. http://dx.doi.org/10.1007/s11242-018-1002-9.

Laban, M., 2020. Hydrogen Storage in Salt Caverns: Chemical Modelling and Analysis of Large-Scale Hydrogen Storage in Underground Salt Caverns (MSc Thesis). TU Delft, pp. 1–86.

Li, D., Cheng, P., Neumann, A., 1992. Contact angle measurement by axisymmetric drop shape analysis (ADSA). Adv. Colloid Interface Sci. 39, 347–382. http://dx.doi.org/10.1016/0001-8686(92)80065-6, URL: https://www.sciencedirect.com/science/article/pii/0001868692800656.

Pan, B., Gong, C., Wang, X., Li, Y., Iglauer, S., 2020. The interfacial properties of clay-coated quartz at reservoir conditions. Fuel 262, 116461.

Pan, B., Yin, X., Ju, Y., Iglauer, S., 2021. Underground hydrogen storage: Influencing parameters and future outlook. Adv. Colloid Interface Sci. 102473. http://dx.doi.org/10.1016/j.cis.2021.102473.

Panfilov, M., Gravier, G., Fillacier, S., 2006. Underground storage of H2 and H2-CO2-CH4 mixtures. In: ECMOR X-10th European Conference on the Mathematics of Oil Recovery. European Association of Geoscientists & Engineers, pp. cp–23.

Peksa, A.E., Wolf, K.-H.A., Zitha, P.L., 2015. Bentheimer sandstone revisited for experimental purposes. Mar. Pet. Geol. 67, 701–719. http://dx.doi.org/10.1016/j.marpetgeo.2015.06.001, URL: https://www.sciencedirect.com/science/article/pii/S0264817215300106.

Pérez, A., Pérez, E., Dupraz, S., Bolcich, J., 2016. Patagonia wind-hydrogen project: underground storage and methanation. In: De 21st World Hydrogen Energy Conference.

RAG, 2017. Underground sun storage. https://www.underground-sun-storage.at/fileadmin/bilder/03_NEU_SUNSTORAGE/Downloads/Underground_Sun.Storage_Publizierbarer_Endbericht_English.pdf.

RAG, 2021. Underground sun storage 2030. https://www.rag-austria.at/forschung-innovation/underground-sun-storage-2030.html.

Ramesh Kumar, K., Makhmutov, A., Spiers, C., Hajibeygi, H., 2021. Geomechanical simulation of energy storage in salt formations. Sci. Rep. 11, 1–24.

Rücker, M., Bartels, W.-B., Singh, K., Brussee, N., Coorn, A., van der Linde, H.A., Bonnin, A., Ott, H., Hassanizadeh, S.M., Blunt, M.J., et al., 2019. The effect of mixed wettability on pore-scale flow regimes based on a flooding experiment in Ketton limestone. Geophys. Res. Lett. 46 (6), 3225–3234. http://dx.doi.org/10.1029/2018GL081784.

Sáinz-García, A., Abarca, E., Grandia, F., 2016. Efficiency and impacts of hythane (CH4+ H2) underground storage. In: EGU General Assembly Conference Abstracts. pp. EPSC2016–16603.

Schaber, C., Mazza, P., Hammerschlag, R., 2004. Utility-scale storage of renewable energy. Electr. J. 17 (6), 21–29.

Simon, J., Férriz, A.M., Correas, L.C., 2015. HyUnder–hydrogen underground storage at large scale: case study Spain. Energy Procedia 73, 136–144.

Stone, H.B.J., Veldhuis, I., Richardson, R.N., 2009. Underground hydrogen storage in the UK. Geol. Soc. Lond. Special Publ. 313 (1), 217–226. http://dx.doi.org/10.1144/SP313.13, arXiv:https://sp.lyellcollection.org/content/313/1/217.full.pdf. URL: https://sp.lyellcollection.org/content/313/1/217.

Tarkowski, R., 2019. Underground hydrogen storage: Characteristics and prospects. Renew. Sustain. Energy Rev. 105, 86–94. http://dx.doi.org/10.1016/j.rser.2019.01.051, URL: http://www.sciencedirect.com/science/article/pii/S1364032119300528.

Taylor, J., Alderson, J., Kalyanam, K., Lyle, A., Phillips, L., 1986. Technical and economic assessment of methods for the storage of large quantities of hydrogen. Int. J. Hydrogen Energy 11 (1), 5–22.

Tek, M.R., 2012. Underground Storage of Natural Gas: Theory and Practice. Vol. 171. Springer Science & Business Media.

van Rooijen, W., Hashemi, L., Farajzadeh, R., Hajibeygi, H., 2021. Microfluidics-based analysis of dynamic contact angles relevant for underground hydrogen storage. Under Rev. X, X.

Walters, A., 1976. Technical and environmental aspects of underground hydrogen storage. In: 1st World Hydrogen Energy Conference. Vol. 2. pp. 2B_65–2B_79.

Yekta, A.E., Manceau, J.C., Gaboreau, S., Pichavant, M., Audigane, P., 2018. Determination of hydrogen–water relative permeability and capillary pressure in sandstone: Application to underground hydrogen injection in sedimentary formations. Transp. Porous Media 122 (2), 333–356. http://dx.doi.org/10.1007/s11242-018-1004-7.

Young, T., 1805. III. An essay on the cohesion of fluids. Philos. Trans. R. Soc. Lond. (95), 65–87.

Zivar, D., Kumar, S., Foroozesh, J., 2021. Underground hydrogen storage: A comprehensive review. Int. J. Hydrogen Energy 46 (45), 23436–23462. http://dx.doi.org/10.1016/j.ijhydene.2020.08.138, URL: https://www.sciencedirect.com/science/article/pii/S0360319920331426. Hydrogen Separation, Production and Storage.